FREQUENCY COMBS

# Observation of topological frequency combs

Christopher J. Flower[1]†, Mahmoud Jalali Mehrabad[1]†, Lida Xu[1]†, Gregory Moille[1], Daniel G. Suarez-Forero[1], Oğulcan Örsel[2], Gaurav Bahl[2], Yanne Chembo[3], Kartik Srinivasan[1], Sunil Mittal[4]*, Mohammad Hafezi[1]*

On-chip generation of optical frequency combs using nonlinear ring resonators has enabled numerous applications of combs that were otherwise limited to mode-locked lasers. Nevertheless, on-chip frequency combs have relied predominantly on single-ring resonators. In this study, we experimentally demonstrate the generation of a novel class of frequency combs, the topological frequency combs, in a two-dimensional lattice of hundreds of ring resonators that hosts fabrication-robust topological edge states with linear dispersion. By pumping these edge states, we demonstrate the generation of a nested frequency comb that shows oscillation of multiple edge state resonances across ≈40 longitudinal modes and is spatially confined at the lattice edge. Our results provide an opportunity to explore the interplay between topological physics and nonlinear frequency comb generation in a commercially available nanophotonic platform.

Nonlinear effects, in particular the Kerr effect, in ring resonators provide a compact route to the generation of optical frequency combs in integrated photonic chips (*1–4*). These combs have led to a plethora of applications including spectroscopy (*5*, *6*), precision timekeeping, on-chip signal synthesis, ranging and detection (*7*, *8*), and optical neural networks. Although Kerr combs have been demonstrated in a wide variety of integrated material platforms, device design has been predominantly limited to single-ring resonators. Coupled resonator systems have only very recently been investigated as a means to engineer the dispersion and, subsequently, the comb spectrum (*9–13*). Beyond dispersion engineering, nonlinear coupled resonator systems can exhibit coherent solutions that are not possible using single-ring resonators (*13–16*).

Concurrently, topological photonics has emerged as a powerful paradigm for the design of photonic devices with novel functionalities (*17–22*). More specifically, topological systems exhibit chiral or helical edge states that are confined to the boundary of the system and are exceptionally robust against imperfections common to integrated photonic devices (*23–25*). Examples include robust optical delay lines (*26*), chiral quantum optics interfaces (*27–29*), slow-light engineering (*30*), waveguides, tapers, and reconfigurable routers (*31–33*). Whereas early efforts in topological photonics focused on linear devices, more recent demonstrations have included nonlinear effects, extending the scope of possible applications to include lasers (*34–37*), parametric amplifiers (*38*, *39*), and quantum light sources (*40–43*). Additionally, it was theoretically shown that nonlinear effects in large two-dimensional (2D) topological arrays of ring resonators can lead to the generation of coherent nested temporal solitons exhibiting an order of magnitude higher efficiency compared with single-ring combs (*44*).

We experimentally demonstrate the generation of the first topological frequency comb in a 2D lattice of >100 ring resonators, fabricated using a commercially available integrated silicon nitride (SiN) nanophotonic platform. As we pump within a topological edge band, we observe the generation of a frequency comb confined within the edge bands across ≈40 longitudinal modes. Using an ultra-high-resolution spectrum analyzer, we reveal the distinctive nested structure of the comb, wherein each comb tooth is further split into a set of finer teeth. Furthermore, we directly image a set of comb teeth and verify that their spatial profile is indeed confined to the edge of the lattice. As such, each comb tooth constitutes a topological edge state that is robust against 90° bends in the lattice and demonstrates the preservation of topology in a highly nonlinear system. This novel modulation instability comb is the first example of a new family of frequency combs and paves the way for the development of coherent topological frequency combs and nested temporal solitons (*44*).

## Design

Our topological system consists of an array of coupled ring resonators that simulates the anomalous quantum Hall (AQH) model for photons (*44–46*), as shown in Fig. 1. The 180 "site-ring" resonators form a square lattice, where nearest and next-nearest sites are coupled together by means of an interspersed lattice of 81 detuned "link-ring" resonators. The link rings are detuned by engineering a path-length difference with respect to the site rings, ensuring that close to site-ring resonances the intensity present in the link rings will be negligible. As a result, the link rings act as waveguides and introduce a direction-dependent hopping phase of $\pm\pi/4$ for nearest-neighbor couplings and 0 for next-nearest neighbor couplings. We note that our system implements a copy of the AQH model at each of the longitudinal mode resonances ($\omega_{0,\mu}$) of the ring resonators. Therefore, the linear dynamics of the system are described by a multiband tight-binding Hamiltonian ($\hat{H}_{\mathrm{L}}$)

$$\begin{aligned}\hat{H}_{\mathrm{L}} = &\sum_{m,\mu}\omega_{0,\mu}\hat{a}^{\dagger}_{m,\mu}\hat{a}_{m,\mu}\\ &-J\sum_{\langle m,n\rangle,\mu}\hat{a}^{\dagger}_{m,\mu}\hat{a}_{n,\mu}e^{-i\phi_{m,n}}\\ &-J\sum_{\langle\langle m,n\rangle\rangle,\mu}\hat{a}^{\dagger}_{m,\mu}\hat{a}_{n,\mu}\end{aligned} \quad (1)$$

Here, $\hat{a}^{\dagger}_{m,\mu}$ is the photon creation operator at a site ring $m$ and longitudinal mode $\mu$. The coupling strength between site rings for both nearest and next-nearest neighbors is given by $J$. The resonance frequency of the site-ring resonators for a longitudinal mode with index $\mu$ is denoted $\omega_{0,\mu} = \omega_0 + D_1\mu + \frac{D_2}{2}\mu^2$, where $D_1$ is the free spectral range (FSR), $D_2$ is the second-order dispersion, and $\omega_0$ is the resonance frequency of the pumped longitudinal mode, $\mu = 0$. This Hamiltonian leads to the existence of an edge band, spectrally located between two bulk bands, near each of the longitudinal mode resonances, as shown in Fig. 1D. Furthermore, simulated transmission shows each edge band hosting another set of resonances. These resonances are associated with the longitudinal modes of the super-ring resonator formed by the edge states, giving rise to a nested mode structure. For the associated band structure, refer to fig. S1.

We also emphasize that the system is time-reversal invariant, and the topological edge states are helical in nature. More specifically, the clockwise (CW) and counterclockwise (CCW) circulation of light in the site rings (also referred to as the pseudospin) leads to edge states that are circulating around the lattice boundary in the CCW and CW directions, respectively. By choosing the port of excitation, we can selectively excite a given edge state (Fig. 1).

In the presence of a strong pump, the intrinsic Kerr nonlinearity of SiN leads to four-wave mixing and, subsequently, the generation of optical frequency combs in the lattice. This nonlinear interaction is described by the following Hamiltonian

$$\hat{H}_{\mathrm{NL}} = -\beta\sum_{m,\mu}\hat{a}^{\dagger}_{m,\mu_1}\hat{a}^{\dagger}_{m,\mu_2}\hat{a}_{m,\mu_3}\hat{a}_{m,\mu_4}\delta_{\mu_1+\mu_2,\mu_3+\mu_4} \quad (2)$$

[1]Joint Quantum Institute, National Institute of Standards and Technology, University of Maryland, College Park, MD, USA. [2]Department of Mechanical Science and Engineering, University of Illinois at Urbana-Champaign, Urbana, IL, USA. [3]Institute for Research in Electronics and Applied Physics, University of Maryland, College Park, MD, USA. [4]Department of Electrical and Computer Engineering, Northeastern University, Boston, MA, USA.
*Corresponding author. Email: s.mittal@northeastern.edu (S.M.); hafezi@umd.edu (M.H.)
†These authors contributed equally to this work.

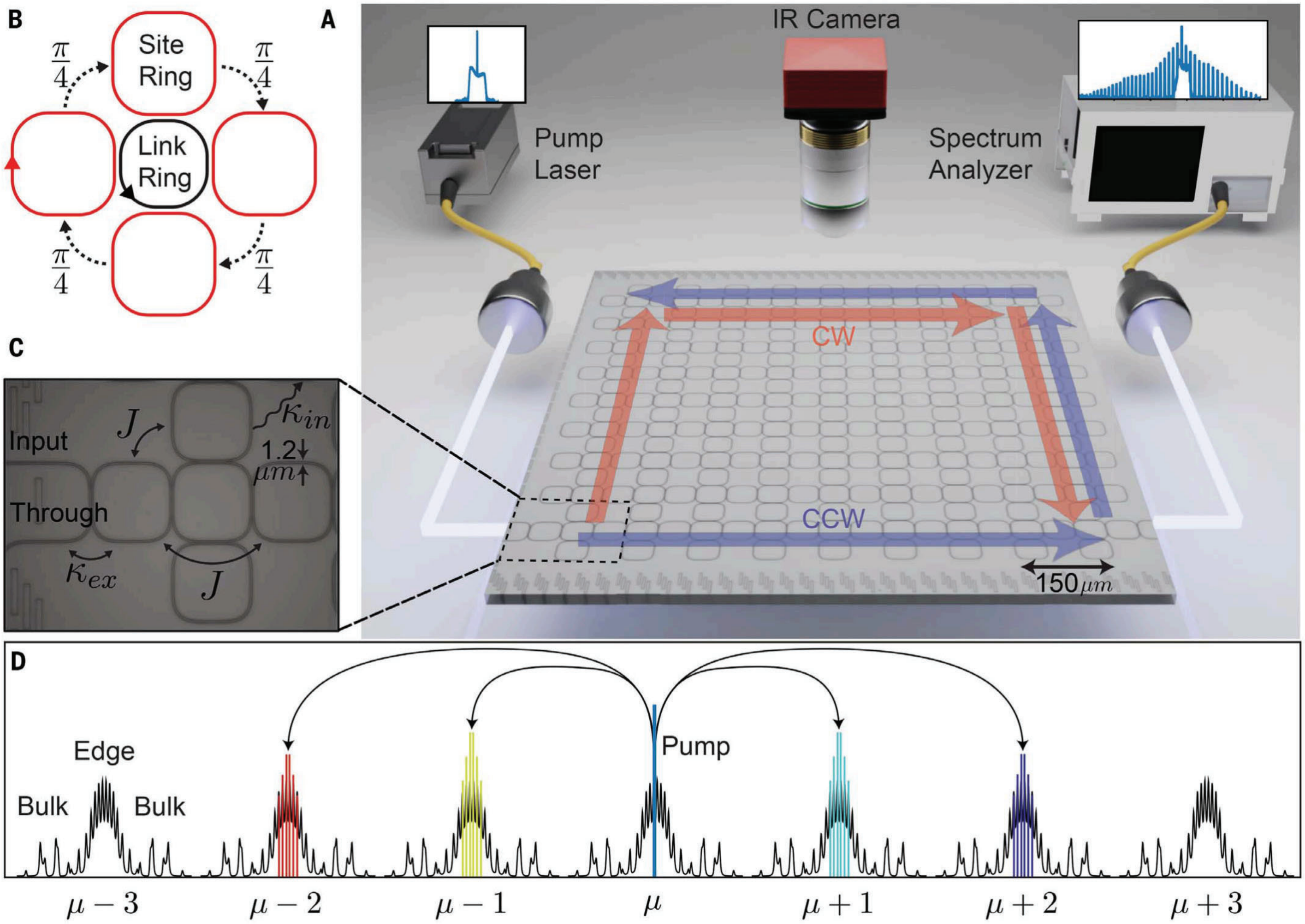


**Fig. 1. Generation of the topological frequency comb.** (**A**) Schematic of the pump, the spectral measurement setup, and an optical image of the device. A tunable pump is coupled into the lattice at the input port and circulates around the edge of the 2D AQH SiN lattice. The generated topological frequency comb spectra are collected from the drop port and analyzed with a spectrum analyzer. The paths followed by CW and CCW edge modes are highlighted in red and blue, respectively. (**B**) Photons acquire a nonzero phase $\pi/4$ when they hop to an adjacent site ring (red) via a link ring (black). (**C**) Close-up high-resolution optical image of the fabricated AQH lattice. Parameters and the input and through ports are marked. (**D**) Simulated linear transmission of the device with the four-wave mixing process schematically depicted.

where $\beta$ is the interaction strength between photons [see the supplementary materials (SM) for definition]. Finally, we note that our lattice is a driven-dissipative system. The dissipation includes both the intrinsic decay rate $\kappa_{in}$ in each individual site and the extrinsic decay rate $\kappa_{ex}$ introduced by the coupling between input or output rings and probe waveguides, as shown Fig. 1. The nonlinear dynamics of this coupled resonator system is described by a modified Lugiato-Lefever formalism that predicts the formation of nested optical frequency combs (*44*). In particular, pumping the lattice in one of the edge bands leads to efficient light generation only in the edge bands centered around other resonances $\omega_{0,\mu}$. This is because the spatial confinement of the edge modes ensures excellent spatial overlap between different edge modes while minimizing overlap between edge and bulk modes. Furthermore, the linear dispersion of the edge modes ensures that the anomalous dispersion from the waveguides is the dominant contribution, as is typical with single-ring combs (*40*, *44*).

#### Device fabrication

This model is experimentally realized in a thick SiN platform patterned through deep-ultraviolet lithography in a commercial foundry (*47*). The device itself consists of a 2D array of 261 coupled photonic ring resonators with two coupled input-output waveguides. A high-resolution optical image in Fig. 1 shows the topological photonic lattice used in this work. The waveguides are embedded in silicon dioxide, and their dimensions are chosen to be 1200 nm wide by 800 nm thick in order to operate in the anomalous dispersion regime. Simulated mode profiles and dispersion can be found in fig. S2 (*48*). Each ring is a racetrack design, composed of 12-μm straight coupling regions and 90° Euler bend regions with a 20 μm effective radius, giving rise to an FSR of ≈0.75 THz. We specifically use Euler bends as opposed to round bends to reduce the mode mixing that occurs at the straight-bent interfaces within each ring (*49*). Although this mode mixing and its impact in perturbing dispersion has also been of concern for single-racetrack combs (*50*), its impact can be physically distinct in our coupled resonator lattice. In particular, spurious hopping phases can be generated through mode conversion during hopping between adjacent rings (*51*). We also note that previous implementations of such topological devices have avoided this problem by operating in the single-mode regime (*46*). The constraints

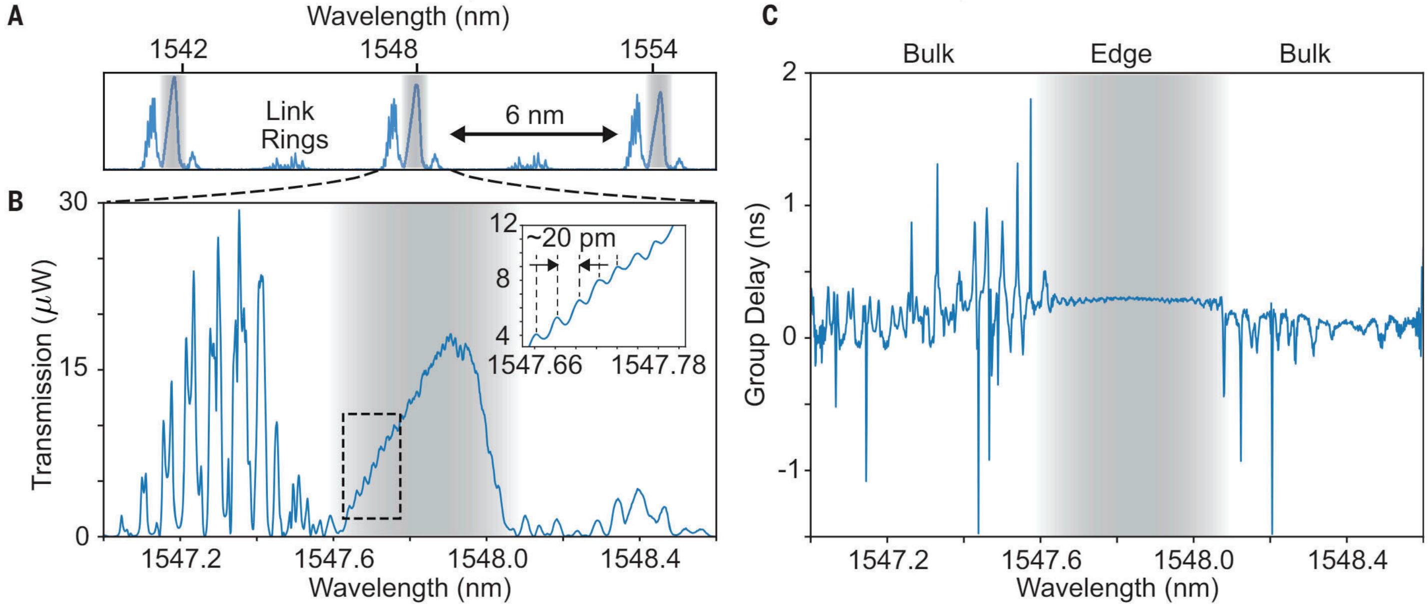


**Fig. 2. Experimental characterization of the topological lattice.** (**A**) Measured drop transmission spectrum of the topological lattice showing bulk and edge bands for three longitudinal modes and detuned link-ring resonances. (**B**) Zoomed drop spectrum of the topological lattice on one set of edge and bulk bands. (**C**) The group delay spectrum showing a flat edge band.

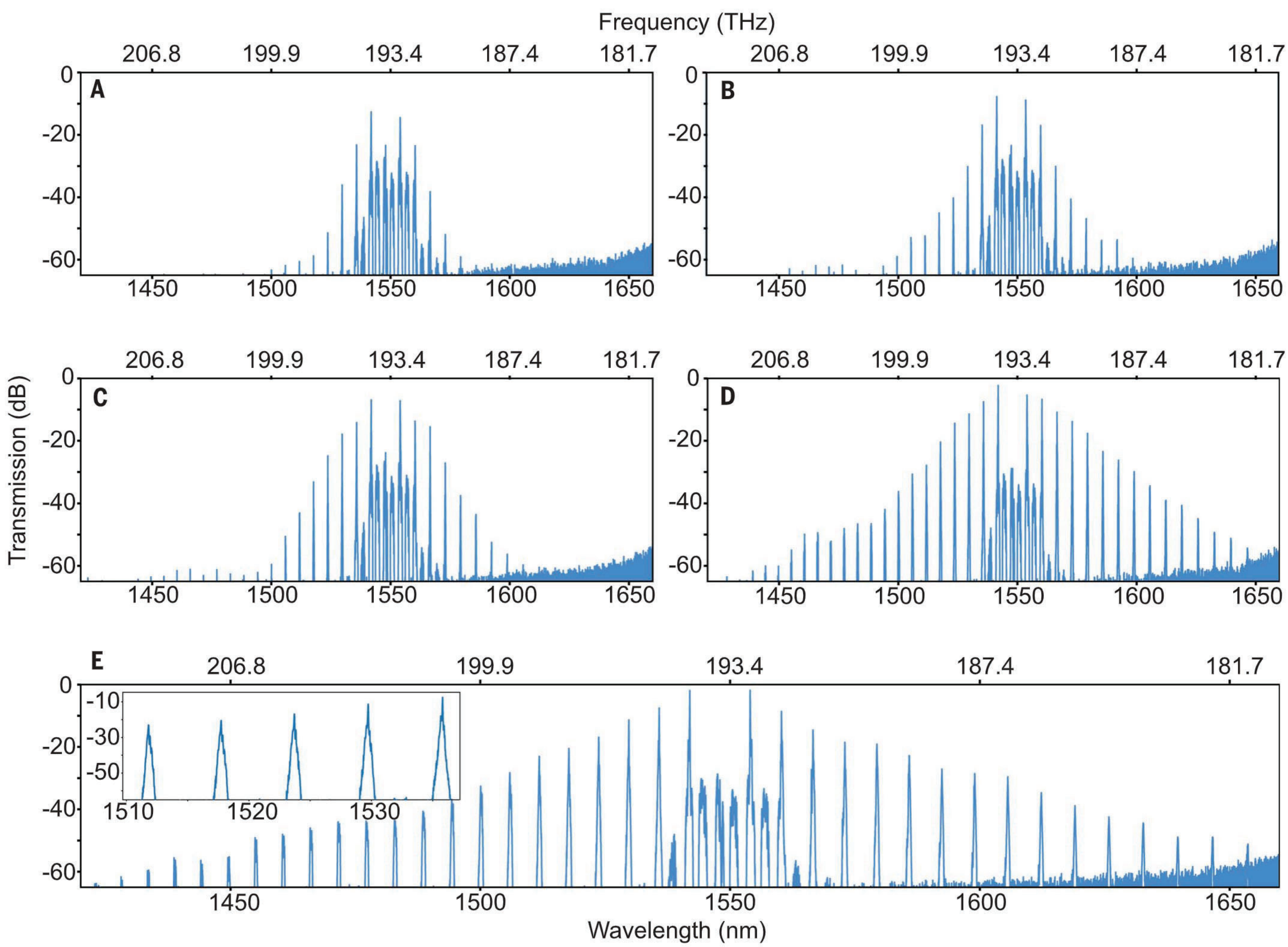


**Fig. 3. Formation of the topological frequency comb.** (**A** to **E**) Comb spectra measured with a pump laser wavelength of 1547.97 nm and peak powers of approximately 70, 78, 86, 92, and 100 W, respectively. The inset in (E) shows a zoomed spectrum of five comb teeth.

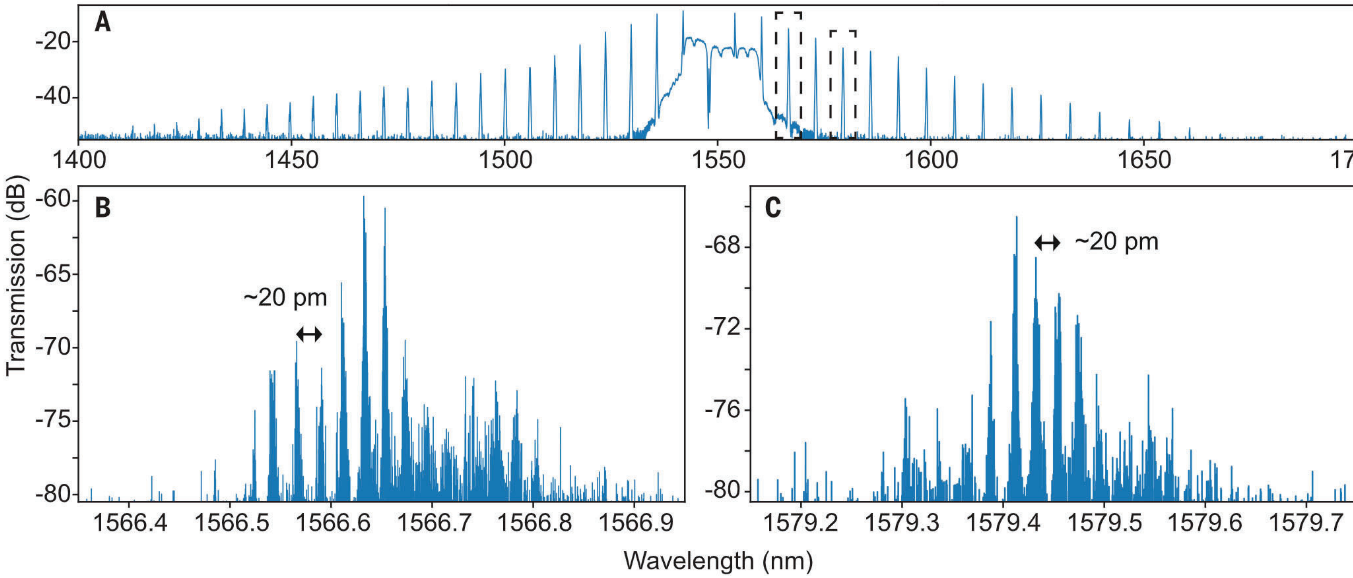


**Fig. 4. High-resolution spectra of individual comb teeth.** (**A**) Low-resolution, broadband comb spectrum with a pump laser wavelength of 1547.97 and on-chip peak power of ~85 W. Individual comb teeth selected for high-resolution analysis are indicated with dashed lines. (**B** and **C**) High-resolution spectra of individual comb teeth showing a nested substructure around 1566.6 and 1579.4 nm, respectively.

placed on waveguide geometry to access anomalous dispersion necessitate the use of wider waveguides that support higher-order modes.

The coupling gaps between the resonators, as well as those between the input-output waveguides and the resonators, are 300 nm, corresponding to an approximate value of $2\pi \times 25$ GHz for the coupling strength, $J$. The extrinsic and intrinsic couplings ($\kappa_{ex}$ and $\kappa_{in}$) are estimated to be $2\pi \times 30$ and $2\pi \times 2$ GHz, respectively (fig. S3). For details on these calculations, see the SM.

### Linear measurements

We begin by characterizing the transmission spectrum of the device in the linear (low-power) regime, where Kerr phase shifts are negligible. Figure 2, A and B, shows the measured drop port transmission spectrum of the device over three longitudinal modes of the site rings, as well as a single higher-resolution spectrum across one transmission band. The edge bands are shaded in gray, and the spacing of the individual edge modes is highlighted in a zoomed inset. While the topological edge states are robust against disorder, the bulk states are prone to reduced transmission. We also note that while the individual edge state resonances in our experiment are not well resolved given that the lattice is strongly coupled to input-output waveguides, the edge mode splitting can be approximated as 20 pm. This is in agreement with the estimated edge bandwidth of the device divided by the number of individual edge modes.

To highlight the linear dispersion of the edge states, we measure the group delay through the lattice (Fig. 2C) using an optical vector analyzer. As expected, the linear dispersion of the edge states leads to a flat group delay response in the edge band, indicating that the dispersion of the super-modes is small, and therefore, the device dispersion is dominated by the single-ring dispersion. The group delay through the bulk states, which do not have a well-defined momentum, shows prominent variations throughout the bulk band.

### Nonlinear measurements

To observe the formation of topological frequency combs in the ring resonator array, we pump the array using a 5-ns pulsed laser with a repetition rate of 250 kHz and on-chip peak powers up to ≈100 W. We specifically choose a long pulse laser with a low duty cycle so that we can achieve a high peak power while keeping the average power low enough to avoid serious thermal effects. Furthermore, the 5-ns pulse duration is longer than any relevant timescale of the lattice dynamics, including the round-trip time in the super-ring resonator (≈400 ps). In other words, the longer pulse duration facilitates a selective quasi-continuous wave excitation of the edge band. We note that operating in this regime is necessary given the particular challenges of fabricating a resonant structure of this scale. See the SM for additional details of these challenges, the nonlinear measurement setup (fig. S4), and the pump laser spectrum (figs. S5 and S6).

We pump the system at the edge band and show the emergence of the topological frequency comb as a function of increasing pump power. In particular, the drop port spectra displayed in Fig. 3 were taken with a pump wavelength of 1547.97 nm and on-chip peak pump powers of 70, 78, 86, 92, and 100 W. We estimate the threshold peak pump power to be ≈70 W, but we also note that the threshold power changes with the pump wavelength. The full comb bandwidth at the highest pump power is ~250 nm wide with about 65 dB contrast from the most prominent sidebands to the noise floor of the measurement. The inset of Fig. 3E shows a zoomed region of the spectrum around 1524 nm, spanning five longitudinal modes. The observed FSR of the comb is ~6 nm, in agreement with the single-ring FSR. For the broadest comb, the contrast between the height of the pump laser and the most prominent sideband (shown in fig. S7) is ~2.9 dB.

To show the nested structure of the topological frequency comb within each comb tooth, we measure the comb output at the through port using an ultra-high-resolution (0.04 pm) heterodyne-based optical spectrum analyzer. A reference low-resolution spectrum is shown in Fig. 4A. We select two individual comb teeth, as indicated, for high-resolution analysis. Within each of these comb teeth, we observe the oscillation of another set of well-resolved modes that correspond to the individual edge modes (Fig. 4, B and C). The spacing between the oscillating edge modes is about 20 pm, which corresponds to the FSR of the super-ring formed by the edge states and agrees with linear measurements. The linewidths of the individual edge modes vary in the range of 3 to 5 pm. For comparison to bulk and single-racetrack comb spectra that lack this nested structure, see fig. S8.

To show that the topological frequency comb inherits the topological properties of the linear system and is indeed confined to the boundary of the lattice, we perform direct imaging of the generated comb. Although the system is designed to confine light in-plane, there is a certain

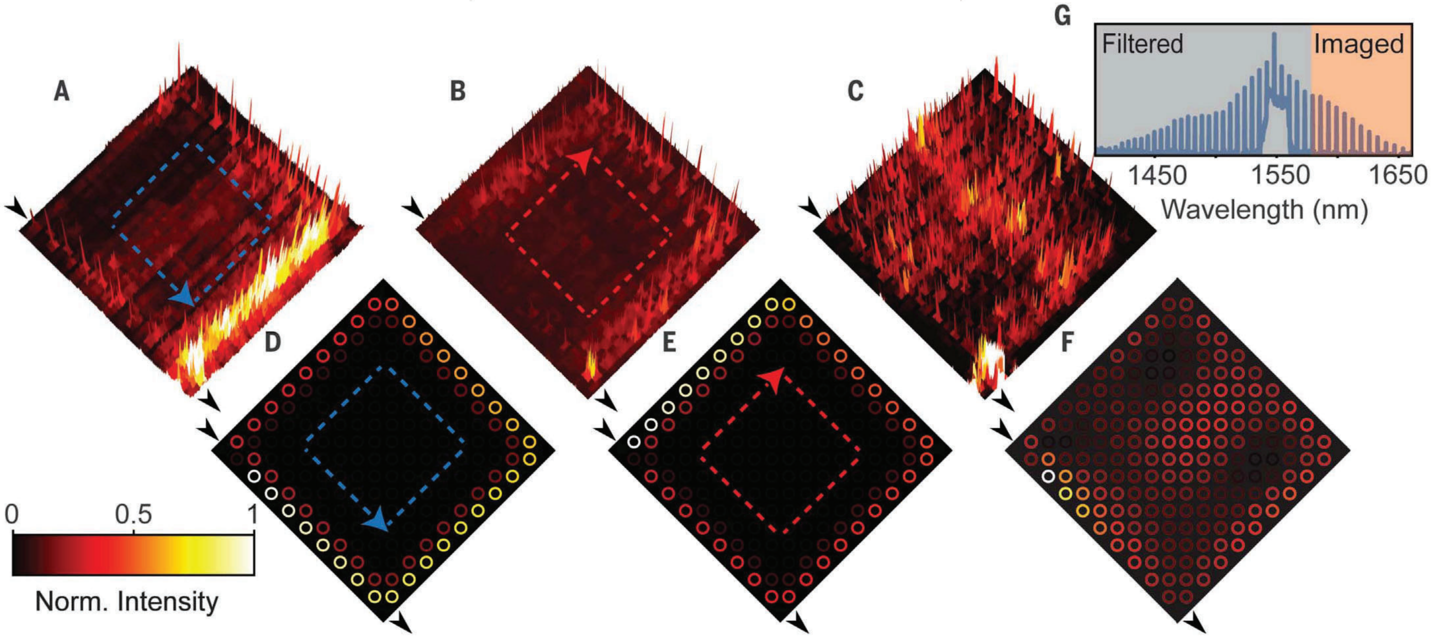


**Fig. 5. Spatial imaging of the topological frequency comb.** (**A** to **C**) Measured spatial imaging of the topological frequency comb for CCW, CW, and bulk modes, respectively. (**D** to **F**) Simulated spatial profile of the CCW, CW, and bulk modes in the linear regime, respectively. (**G**) The integration bandwidth used for the top-down imaging.

amount of out-of-plane scattering caused by fabrication imperfections and disorder. The light scattered as a result of surface roughness is collected from above with a 10× objective lens and imaged on an infrared (IR) camera. In addition, we use a 1580-nm long-pass filter to remove the pump and only collect part of the generated comb light.

Figure 5 shows the measured spatial intensity profile of three types of generated frequency combs. First, we observe that the generated comb light is confined to the edge of the lattice and that light travels from the input to the output port in the CCW direction. Note that the lattice is not critically coupled to the bus waveguides, therefore the light continues to circulate around the lattice after reaching the first output port in its path. Moreover, the propagation is robust, and no noticeable scattering into the bulk is observed from the two sharp 90° corners. These characteristics show that the comb teeth are indeed generated within the topological edge band and that the topology is preserved even in the presence of strong nonlinearity.

Next, by pumping the system in the other pseudospin, we generate the comb in the CW edge state. We observe similar confinement of the topological frequency comb, but here the light travels in the opposite direction around the lattice, as expected.

In sharp contrast to the CW and CCW edge band excitation, when we excite the lattice in the bulk band, the spatial intensity distribution of generated frequencies exhibits no confinement and occupies the bulk of the lattice. These images represent a novel look into the spatial profile of frequency comb formation, enabled by the distinctive geometry and scale of the topological lattice. For the spectra (fig. S9) and details on the generation of each of these types of frequency combs, see the SM. Additionally, Fig. 5 shows simulated spatial distributions of CCW, CW, and bulk modes in the linear regime for comparison, as well as a schematic illustrating the filtered and imaged regions of the spectrum. We note that in these linear simulation results, we observe a uniform decay in intensity due to propagation loss from the input to the output port. In contrast, our experimentally observed intensity profiles do not show a uniform decay, likely because of competition between the linear loss and the nonlinear parametric gain. For a comparison with nonlinear simulation results, see fig. S10.

## Outlook

Here we have demonstrated the first topological frequency comb using an array of >100 coupled resonators. Our results entail the first realization of a new class of frequency combs that also includes coherent dissipative solutions, such as nested solitons and phase-locked Turing rolls, that are not accessible using single resonators (*44*). The distinctive nested spectral structure of these combs, characterized by two disparate frequency scales, could lead to a host of new applications. For instance, this nested structure could be useful in certain spectroscopic measurements where there are multiple regions of interest that each require a high-resolution analysis but are separated by a large frequency gap. Moreover, in this work, we have used a commercially available SiN platform in order to operate in the telecom wavelength regime. However, our device design can be easily translated to other frequency domains and photonic material platforms that can exhibit much higher nonlinearities, such as aluminum gallium arsenide (*52*, *53*) and lithium niobate (*54*).

On a more fundamental level, our results provide a new platform to study the interplay of topology and optical nonlinearities (*21*, *55*, *56*), as well as intriguing topological physics specific to bosons. For example, although optical nonlinearities have been used to demonstrate topological phase transitions and restructured bulk-edge correspondence (*57*, *58*), in this work we observe that the system retains the topological behavior of its linear counterpart even in the presence of such strong nonlinear effects. These results could enable novel applications where topological physics is used to engineer the underlying band structure (or dispersion) of a linear system and optical nonlinearities provide additional functionalities.

### REFERENCES AND NOTES


1. T. J. Kippenberg, R. Holzwarth, S. A. Diddams, *Science* **332**, 555–559 (2011).
2. A. Pasquazi *et al.*, *Phys. Rep.* **729**, 1–81 (2018).
3. A. L. Gaeta, M. Lipson, T. J. Kippenberg, *Nat. Photonics* **13**, 158–169 (2019).
4. S. A. Diddams, K. Vahala, T. Udem, *Science* **369**, eaay3676 (2020).
5. M.-G. Suh, Q.-F. Yang, K. Y. Yang, X. Yi, K. J. Vahala, *Science* **354**, 600–603 (2016).
6. D. A. Long *et al.*, *Nat. Photonics* **18**, 127–131 (2024).
7. J. Riemensberger *et al.*, *Nature* **581**, 164–170 (2020).
8. R. Chen *et al.*, *Nat. Photonics* **17**, 306–314 (2023).
9. S. A. Miller *et al.*, *Opt. Express* **23**, 21527–21540 (2015).
10. S. Kim *et al.*, *Nat. Commun.* **8**, 372 (2017).

11. H. Bao *et al.*, *Nat. Photonics* **13**, 384–389 (2019).
12. X. Xue, X. Zheng, B. Zhou, *Nat. Photonics* **13**, 616–622 (2019).
13. Z. Yuan *et al.*, *Nat. Photonics* **17**, 977–983 (2023).
14. J. Vasco, V. Savona, *Phys. Rev. Appl.* **12**, 064065 (2019).
15. A. Tikan *et al.*, *Nat. Phys.* **17**, 604–610 (2021).
16. A. Tusnin, A. Tikan, K. Komagata, T. J. Kippenberg, *Commun. Phys.* **6**, 317 (2023).
17. L. Lu, J. D. Joannopoulos, M. Soljačić, *Nat. Photonics* **8**, 821–829 (2014).
18. T. Ozawa *et al.*, *Rev. Mod. Phys.* **91**, 015006 (2019).
19. H. Price *et al.*, *JPhys Photonics* **4**, 032501 (2022).
20. X. Zhang, F. Zangeneh-Nejad, Z.-G. Chen, M.-H. Lu, J. Christensen, *Nature* **618**, 687–697 (2023).
21. D. Smirnova, D. Leykam, Y. Chong, Y. Kivshar, *Appl. Phys. Rev.* **7**, 021306 (2020).
22. M. Jalali Mehrabad, S. Mittal, M. Hafezi, *Phys. Rev. A* **108**, 040101 (2023).
23. Z. Wang, Y. Chong, J. D. Joannopoulos, M. Soljacić, *Nature* **461**, 772–775 (2009).
24. M. C. Rechtsman *et al.*, *Nature* **496**, 196–200 (2013).
25. M. Hafezi, S. Mittal, J. Fan, A. Migdall, J. M. Taylor, *Nat. Photonics* **7**, 1001–1005 (2013).
26. S. Mittal *et al.*, *Phys. Rev. Lett.* **113**, 087403 (2014).
27. S. Barik *et al.*, *Science* **359**, 666–668 (2018).
28. M. Jalali Mehrabad *et al.*, *Optica* **10**, 415 (2023).
29. S. Guddala *et al.*, *Science* **374**, 225–227 (2021).
30. J. Guglielmon, M. C. Rechtsman, *Phys. Rev. Lett.* **122**, 153904 (2019).
31. M. I. Shalaev, W. Walasik, A. Tsukernik, Y. Xu, N. M. Litchinitser, *Nat. Nanotechnol.* **14**, 31–34 (2019).
32. C. J. Flower *et al.*, *ACS Photonics* **10**, 3502–3507 (2023).
33. H. Zhao *et al.*, *Science* **365**, 1163–1166 (2019).
34. P. St-Jean *et al.*, *Nat. Photonics* **11**, 651–656 (2017).
35. B. Bahari *et al.*, *Science* **358**, 636–640 (2017).
36. M. A. Bandres *et al.*, *Science* **359**, eaar4005 (2018).
37. L. Yang, G. Li, X. Gao, L. Lu, *Nat. Photonics* **16**, 279–283 (2022).
38. V. Peano, M. Houde, F. Marquardt, A. A. Clerk, *Phys. Rev. X* **6**, 041026 (2016).
39. B.-U. Sohn *et al.*, *Nat. Commun.* **13**, 7218 (2022).
40. S. Mittal, E. A. Goldschmidt, M. Hafezi, *Nature* **561**, 502–506 (2018).
41. A. Blanco-Redondo, B. Bell, D. Oren, B. J. Eggleton, M. Segev, *Science* **362**, 568–571 (2018).
42. S. Mittal, V. V. Orre, E. A. Goldschmidt, M. Hafezi, *Nat. Photonics* **15**, 542–548 (2021).
43. T. Dai *et al.*, *Nat. Photonics* **16**, 248–257 (2022).
44. S. Mittal, G. Moille, K. Srinivasan, Y. K. Chembo, M. Hafezi, *Nat. Phys.* **17**, 1169–1176 (2021).
45. D. Leykam, S. Mittal, M. Hafezi, Y. D. Chong, *Phys. Rev. Lett.* **121**, 023901 (2018).
46. S. Mittal, V. V. Orre, D. Leykam, Y. D. Chong, M. Hafezi, *Phys. Rev. Lett.* **123**, 043201 (2019).
47. A. Rahim *et al.*, *IEEE J. Sel. Top. Quantum Electron.* **25**, 1–18 (2019).
48. K. Luke, Y. Okawachi, M. R. E. Lamont, A. L. Gaeta, M. Lipson, *Opt. Lett.* **40**, 4823–4826 (2015).
49. T. Fujisawa, S. Makino, T. Sato, K. Saitoh, *Opt. Express* **25**, 9150–9159 (2017).
50. X. Ji *et al.*, *Commun. Phys.* **5**, 84 (2022).
51. L. D. Tzuang, K. Fang, P. Nussenzveig, S. Fan, M. Lipson, *Nat. Photonics* **8**, 701–705 (2014).
52. L. Chang *et al.*, *Nat. Commun.* **11**, 1331 (2020).
53. M. Pu, L. Ottaviano, E. Semenova, K. Yvind, *Optica* **3**, 823 (2016).
54. M. Zhang *et al.*, *Nature* **568**, 373–377 (2019).
55. M. Jürgensen, S. Mukherjee, M. C. Rechtsman, *Nature* **596**, 63–67 (2021).
56. N. Mostaan, F. Grusdt, N. Goldman, *Nat. Commun.* **13**, 5997 (2022).
57. L. J. Maczewsky *et al.*, *Science* **370**, 701–704 (2020).
58. M. S. Kirsch *et al.*, *Nat. Phys.* **17**, 995–1000 (2021).
59. C. J. Flower *et al.*, Observation of Topological Frequency Combs [Dataset], Dryad (2024); https://doi.org/10.5061/dryad.xwdbrv1mw.

## ACKNOWLEDGMENTS

The authors acknowledge fruitful discussions with E. Goldschmidt, A. Dutt, R. Vasanth, D. Session, and E. Mechtel. **Funding:** This work was supported by Airforce Office of Scientific Research grant FA9550-22-1-0339, Office of Naval Research grant N00014-20-1-2325, Army Research Lab grant W911NF1920181, National Science Foundation grant DMR-2019444, and the Minta Martin and Simons Foundations. **Author contributions:** C.J.F. designed the devices and constructed the experimental setup. C.J.F. performed the measurements, with assistance from L.X. and M.J.M. C.J.F. and L.X. performed the simulations. C.J.F., L.X., and M.J.M. analyzed the data. All work was supervised by G.M., K.S., S.M., and M.H. All authors discussed the results and contributed to the manuscript. **Competing interests:** S.M. and M.H. are inventors on a patent (US Patent 11599006) dated 7 March 2023 that covers the generation of nested frequency combs in a topological source. The authors declare that they have no other competing interests. **Data and materials availability:** All data needed to evaluate the conclusions in the paper are present in the figures of the paper and/or the supplementary materials. The data can also be accessed at Dryad (*59*). 

## SUPPLEMENTARY MATERIALS

science.org/doi/10.1126/science.ado0053
Supplementary Text
Figs. S1 to S10
Reference (*60*)

Submitted 11 January 2024; accepted 9 May 2024
10.1126/science.ado0053

Science
AAAS

# Supplementary Materials for

## **Observation of topological frequency combs**

Christopher J. Flower *et al*.

Corresponding authors: Sunil Mittal, s.mittal@northeastern.edu; Mohammad Hafezi, hafezi@umd.edu

*Science* **384**, 1356 (2024)
DOI: 10.1126/science.ado0053

**The PDF file includes:**

Supplementary Text
Figs. S1 to S10
References

# Band Structure

Figure S1 shows the calculated band structure of a semi-infinite (periodic in one axis, finite in the other) AQH lattice. A $2J$-wide edge band region (highlighted in grey) resides between two bulk bands. Unlike the bulk modes, which lack well-defined momentum, there are two unidirectional edge bands with opposite pseudospins. These bands travel in opposite directions and are robust against local disorder (*45, 46*). Additionally, the lattice unit cell is depicted schematically.

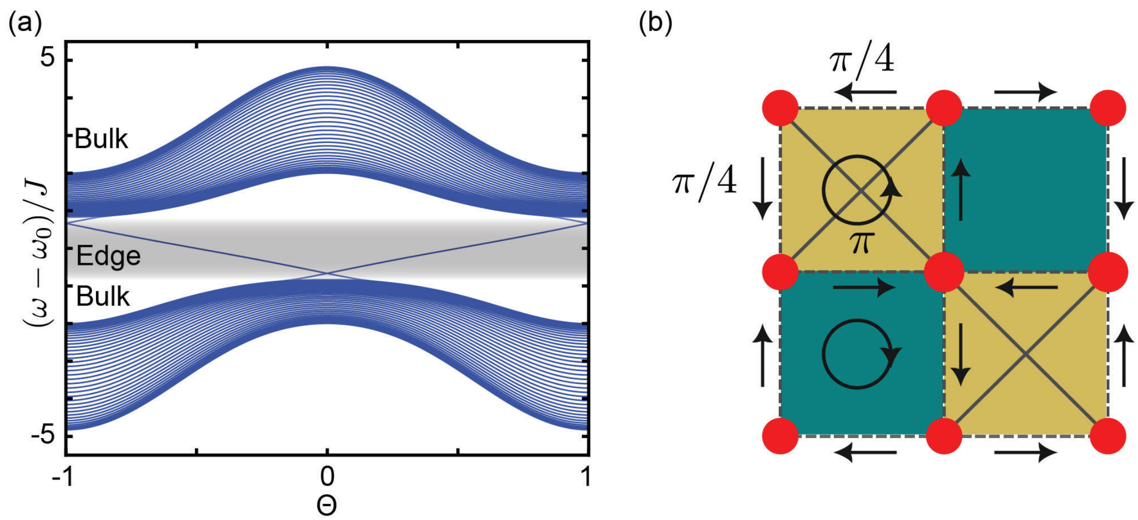


Figure S1: **Band Structure.** (a) The band structure of a semi-infinite lattice (finite along the y-axis, periodic boundary conditions along the x-axis). Here $\Theta$ is the phase between neighboring site-rings along the axis with periodic boundary conditions. The edge band is highlighted in grey. (b) A schematic of the unit cell of the lattice.

# Estimation of Device Parameters

In our second quantized formalism, the strength of interaction $\beta$ is related to the effective Kerr nonlinear strength $\gamma$ common in the literature as $\gamma = \frac{\beta}{\hbar\omega}\frac{n_0^2 L_{\text{eff}}}{c^2}$, where $n_0$ is the refractive index, $L_{\text{eff}}$ is the circumference of the individual ring, and $\omega_0$ is the pump frequency. In order to estimate $\gamma$, we also require the nonlinear index $n_2$ and the effective mode area $A_{\text{eff}}$. Here, a value of $n_2 = 2.4 \times 10^{-19}$ m$^2$ W$^{-1}$ is used (*60*). The refractive index of SiN at a wavelength of 1550 nm is taken as $n_0 = 2.00$ (*48*). A value of $A_{\text{eff}} = 0.9 \times 10^{-12}$ m$^2$ was calculated using FDTD simulation and $L_{\text{eff}} = 174\ \mu$m. With these values, we calculate $\gamma$ as:

$$\gamma = \frac{\omega_0 n_2}{c A_{\text{eff}}} = 1.08\ \text{W}^{-1}\text{m}^{-1} \tag{S1}$$

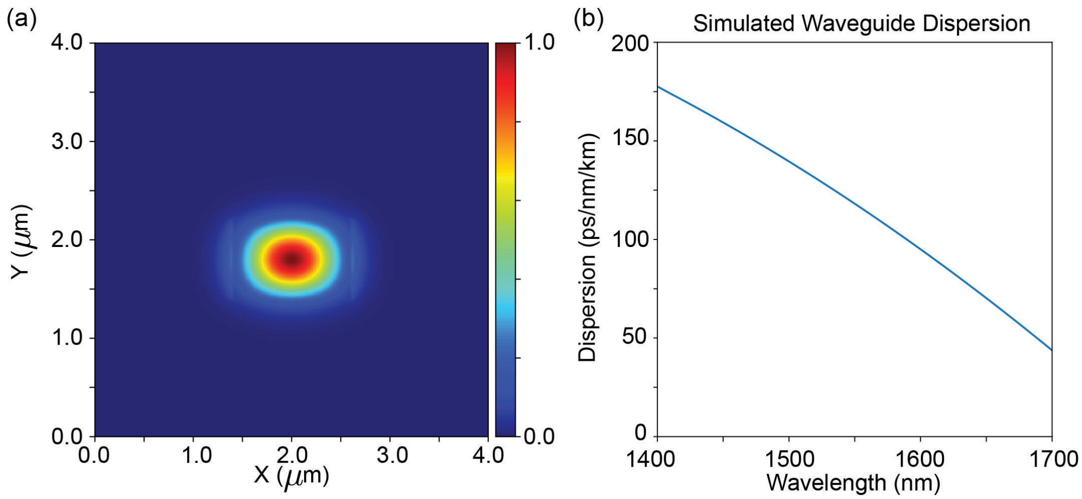


Figure S2: **Modal cross-section.** (a) Simulated electric field intensity in normalized units for a SiN waveguide cross-section of 1200 nm wide by 800 nm thick. Embedded in $SiO_2$ cladding. (b) Simulated dispersion profile for the waveguide.

We note that the definition of effective Kerr nonlinear strength $\gamma$ in this paper is common in the literature but differs from what was used in reference (*44*), in which it was taken as $\omega_0 c n_2 / n_0^2 V_{\text{eff}}$. The simulated mode profile and dispersion are displayed in Figure S2, using the dependence of the refractive index on wavelength reported in (*48*).

The relevant parameters used in theoretical modeling are estimated from our device as follows. $J$, the coupling strength between rings is estimated by comparing the measured drop spectrum of the lattice with simulation in the linear regime. The full bandwidth of edge and bulk bands is estimated to be approximately $8J$ in simulation, while the edge band alone is approximately $2J$. Using this, we arrive at an estimate of $J \approx 2\pi \times 25$ GHz for our device. In order to approximate the splitting of individual edge modes, we divide the bandwidth ($2J$) by the number of individual edge modes given the size of the lattice (20). This yields a splitting of $2\pi \times 2.5$ GHz, which is 20 pm.

The extrinsic coupling rate $\kappa_{\text{ex}}$ and the intrinsic decay rate $\kappa_{\text{in}}$ are estimated based on single-rings coupled to two waveguides, also known as add-drop filters (ADFs). Using the single-mode approximation, the transmission spectrum of the through port of an ADF with a given $\kappa_{\text{ex}}$ and $\kappa_{\text{in}}$ is a Lorentzian function:

$$T = \frac{(\omega - \omega_0)^2 + (\kappa_{\text{ex}}^{\text{O}} - \kappa_{\text{ex}}^{\text{I}} + \kappa_{\text{in}})^2}{(\omega - \omega_0)^2 + (\kappa_{\text{ex}}^{\text{O}} + \kappa_{\text{ex}}^{\text{I}} + \kappa_{\text{in}})^2}. \tag{S2}$$

Here $\kappa_{\text{ex}}^{\text{I}}$ ($\kappa_{\text{ex}}^{\text{O}}$) is the extrinsic coupling to the input (output) waveguide. In the case of our lattice, due to identical coupling gaps, $\kappa_{\text{ex}}^{\text{I}} = \kappa_{\text{ex}}^{\text{O}} = \kappa_{\text{ex}}$. By measuring the transmission from the through port (see Figure S3) and fitting the curve to the above Lorentzian we extract the values $\kappa_{\text{ex}} \approx 2\pi \times 30$ GHz and $\kappa_{\text{in}} \approx 2\pi \times 2$ GHz. This corresponds to a single-ring loaded

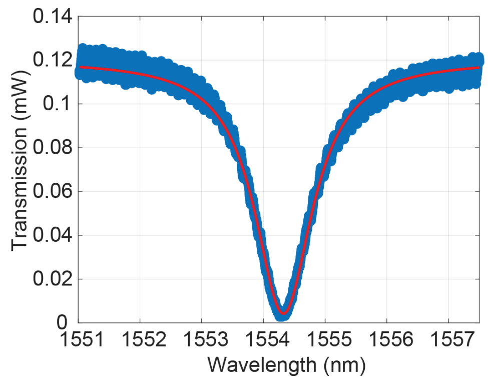


Figure S3: **Through spectrum of an ADF around one resonance.** Blue: Experimental data. Red: Lorentzian fitting.

quality factor of about 1500, and an intrinsic quality factor of about 50,000.

We note that the relatively low quality factor is a result of the large value of $J$. This value is chosen in particular due to the role of disorder in the fabrication, which results in the detuning of the resonance frequencies of rings with identical parameters. Specifically, our topological devices are robust as long as the disorder in ring resonance frequencies is small compared to the width of the topological bandgap (2J). Additionally, topological lattices of this nature have been shown to be more robust to fabrication disorder than other systems, such as 1D chains of rings (*26*). While frequency comb generation has been studied theoretically in 1D chains of rings (*16*), such structures are expected to be highly susceptible to fabrication disorder.

A propagation loss of -6.2 dB through the topological edge band in the CW direction through the lattice is estimated by comparing the through port off-resonant transmission with the on-resonant drop port transmission in the linear regime.

# Measurement Setup and Methods

For measurements in the linear regime, we couple a continuous-wave tunable laser to the input port (via edge couplers) and sweep the wavelength. Concurrently, the output power is measured at the drop port across the lattice with a power meter. For the measurement of the group delay of the drop port transmission, we use an optical vector network analyzer. In both cases, polarization is controlled with a standard 3-paddle polarization controller at the laser output.

A schematic of the experimental setup for nonlinear measurement is shown in Figure S4. For these measurements, we couple a pulsed tunable laser to a free-space optical setup including a variable attenuator and a polarization controller comprised of a quarter, half, and quarter waveplate. The output is then coupled into a short tapered fiber and edge coupled into the SiN chip via the input port. Coupling losses are estimated to be 2-3 dB per coupler. The pump and comb output are collected from the drop port with another tapered fiber and optionally attenuated or

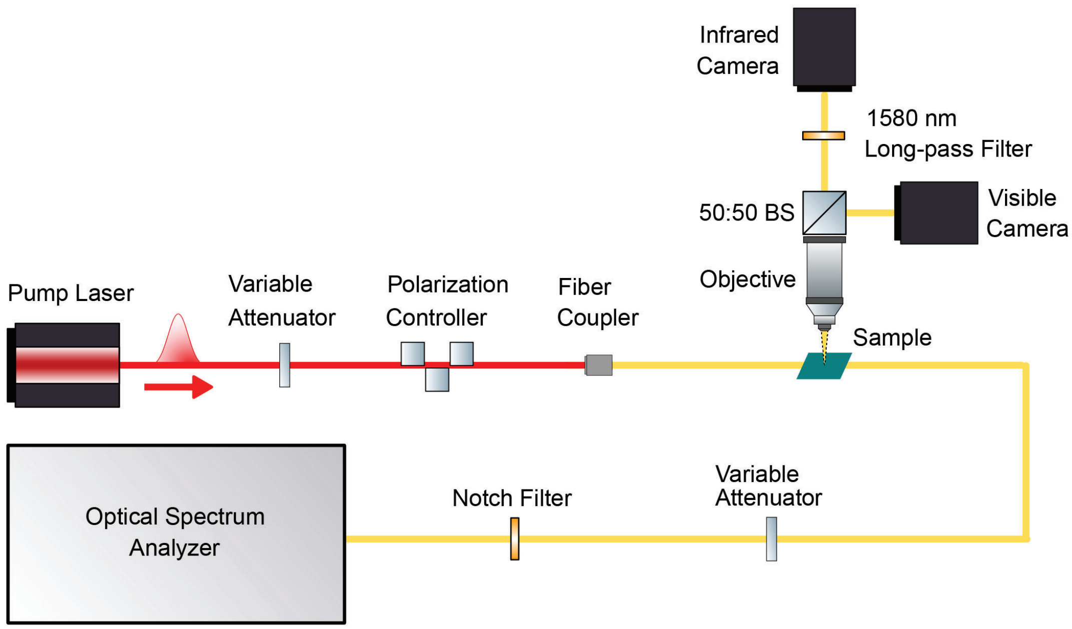


Figure S4: **Detailed schematic of the nonlinear measurement setup.** A tunable telecom pulsed laser is sent through a variable attenuator and polarization controller before being fiber-coupled and sent into the SiN device. The output of the device is then fiber-coupled and optionally attenuated by a second variable attenuator and notch filter for pump removal before being sent to the Optical Spectrum Analyzer. The chip is also imaged from above with a 10x objective, followed by a 50:50 beamsplitter. One optical path is sent to a visible camera, while the other is filtered by a 1580 nm long-pass filter and sent to an IR-sensitive camera.

filtered prior to being sent into an optical spectrum analyzer.

For imaging, we collect out-of-plane scattering from the SiN chip with a 10x objective lens with a numerical aperture of 0.28. The image is sent through a 50:50 beamsplitter to a visible wavelength camera as well as an infrared (IR) sensitive camera. A 1580 nm long-pass filter is included prior to the IR camera to filter out the pump laser.

# Pump Laser Characterization

The pump laser used in the nonlinear measurements described in this work is a tunable pulsed laser. The pulse duration is designed to be approximately 5 ns with a repetition rate of 250 kHz. This relatively long pulse duration (compared to the longest timescales of the lattice dynamics) and low repetition rate provide access to a high power quasi-continuous wave regime. In particular, operation in this regime allows power requirements to be satisfied and detrimental thermal effects to be minimized while numerical modeling using a single frequency pump remains applicable.

Three pump laser spectra are shown in Figure S5 for three different central wavelengths. As can be seen, the laser background remains approximately 30 dB suppressed from the laser peak regardless of the pump central wavelength. The spectral linewidth of the pump is approximately 3 pm.

The same laser envelope can be observed when sending the pump through a topological lattice and collecting the drop port spectrum. The output spectrum of an identical AQH lattice as the one used in the nonlinear measurements in this work with a pump power below the comb formation threshold is shown in Figure S6. The broad laser background is transmitted through several edge bands as well as link-ring bands, producing a characteristic structure that can be observed in the main text.

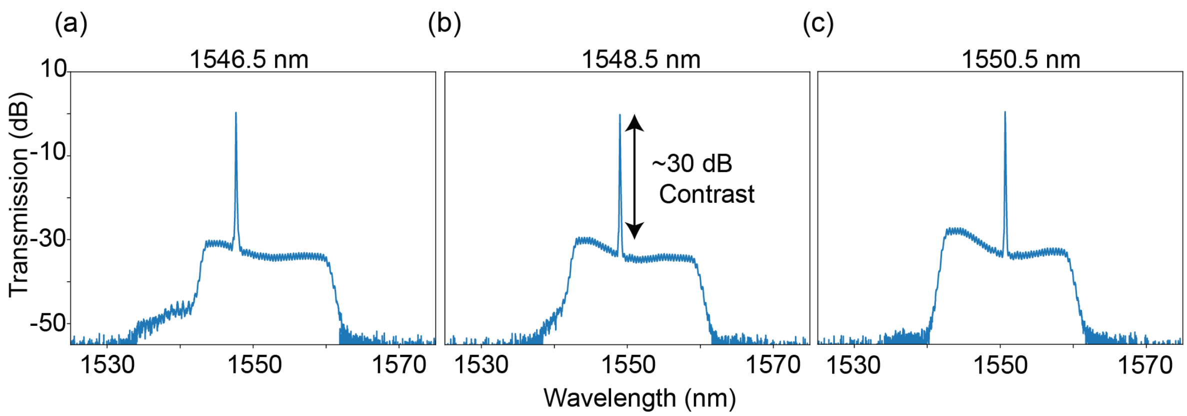


Figure S5: **Laser characterization.** The unfiltered spectrum of the pump laser at approximately (a) 1546.5 nm, (b) 1548.5 nm, (c) and 1550.5 nm.

# Comb Contrast

Figure S7 shows a reference spectrum comparable to that of Fig. 3e with the pump laser included.

# Nesting Comparison

In order to contrast the high-resolution spectra in Fig. 4 with more typical, non-nested frequency combs, we generate a bulk comb as described in the main text, as well as a frequency comb in a single-racetrack resonator with identical dimensions as the site-ring resonators in the topological lattice, shown in Figure S8. The on-chip peak power used for the bulk comb is

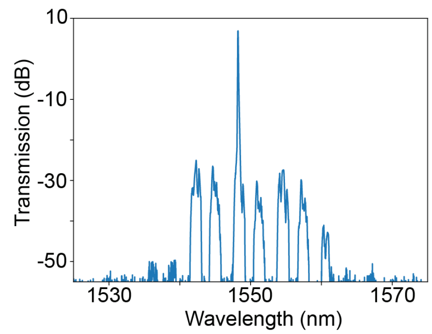


Figure S6: **Laser background drop spectrum.** The output drop spectrum of an AQH lattice when the pump is detuned and below the comb formation threshold.

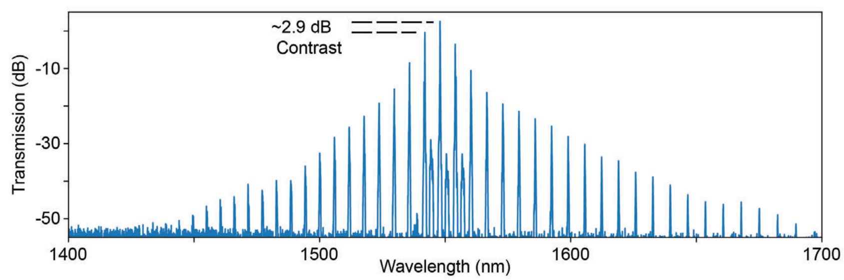


Figure S7: **Comb Contrast.** Spectrum of a topological frequency comb comparable to that of Fig. 3e with the pump laser included.

approximately 122 W with a pump wavelength of 1547.43 nm. The single-racetrack resonator is coupled in an add-drop filter configuration, where there are two bus waveguides. Notably, the coupling gaps here are increased from 300 nm to 600 nm in order to increase the loaded Q factor from $\approx 1500$ to $\approx 21,000$. For the single-racetrack comb, the pump wavelength is 1547.32 nm and the peak power is approximately 104 W. Linewidths for the main peaks of each comb tooth are approximately 3 pm, 13 pm, and 18 pm respectively.

# Generation and Spectra of Imaged Modes

For the CCW and CW topological frequency comb images in Fig. 5, the peak pump power in the waveguide was approximately 92 W and 100 W respectively. The wavelength was tuned through the edge band to a value of 1547.97 nm. In order to generate a bulk comb, the peak pump power in the waveguide was approximately 125 W and the laser was tuned onto resonance with a bulk mode at 1547.43 nm. Through port spectra of each of these combs are displayed in Figure S9. We note that while the pump power used here for the bulk mode is significantly higher than that of the topological combs, a broader systematic study would be required to

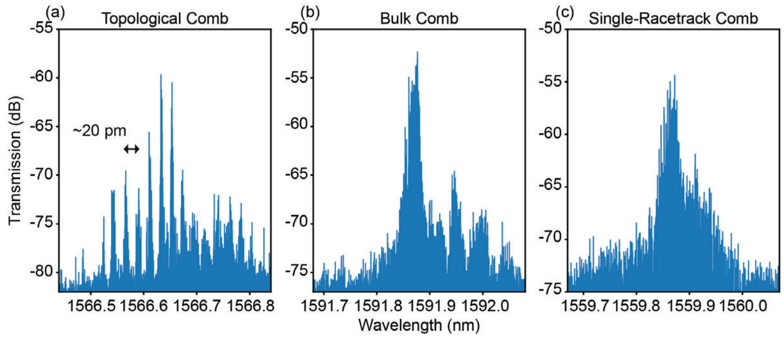


Figure S8: **High-Resolution Spectra of Individual Comb Teeth.** (a) A high-resolution comb tooth from the topological frequency comb, displaying nesting. (b) A high-resolution comb tooth from a bulk comb. (c) A high-resolution comb tooth from a single-racetrack comb.

determine the minimum power required to generate frequency combs in bulk modes of the lattice. Due to the highly variable nature of these bulk modes, such a study is outside the scope of the present work.

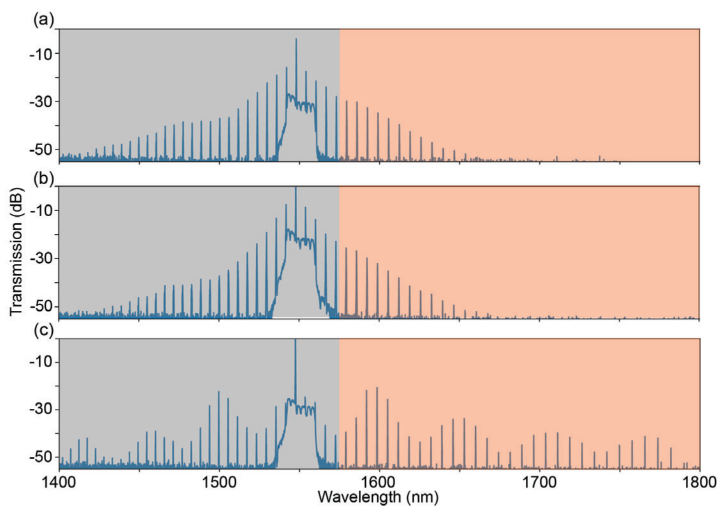


Figure S9: **CCW, CW, and bulk comb spectra.** The generated comb spectrum when the pump is tuned in resonance with a (a) CCW mode, (b) CW mode, and (c) bulk mode. Filtered wavelengths are highlighted in grey, while imaged wavelengths are highlighted in red.

## Simulated Nonlinear Mode Profiles

Mode profiles for four pump detuning values, simulated as outlined in Ref. (44), but with realistic device parameters, are displayed in Fig. S10. Additionally, only comb teeth at wavelengths longer than 1580 nm are displayed in order to more closely replicate the experimental data. In particular, panels (a) and (b) show two topological frequency comb profiles with pump wavelengths within the edge band (with detunings of 0.70 and 0.65 $J$ from the center of the edge band, respectively). As can be seen, the intensity is confined to the lattice edge in both cases, but the uniform intensity profile seen in linear simulations is not necessarily maintained. Panels (c) and (d) show two additional comb profiles where the pump wavelength lies within the bulk region (with pump detunings of 1.39 and 1.34 $J$, respectively).

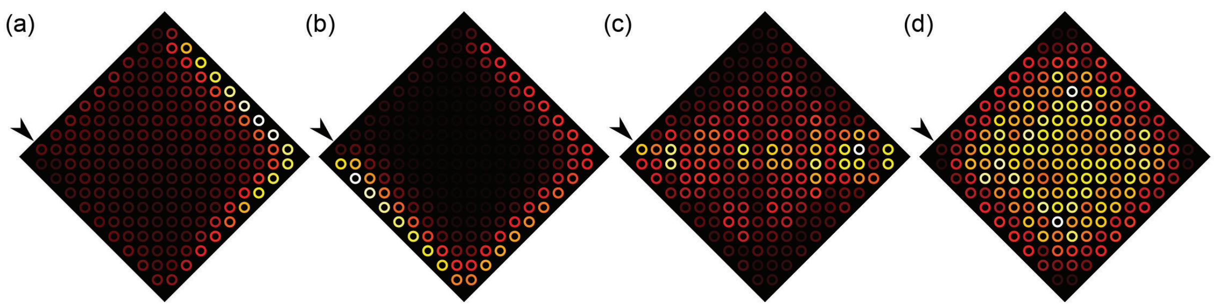


Figure S10: **Simulated nonlinear mode profiles.** (a,b) Simulated topological frequency comb mode profiles for two different pump detunings within the edge band. (c,d) Simulated frequency comb mode profiles for two different pump detunings within the bulk band.

## References and Notes


1. T. J. Kippenberg, R. Holzwarth, S. A. Diddams, Microresonator-based optical frequency combs. *Science* **332**, 555–559 (2011). doi:10.1126/science.1193968 Medline

2. A. Pasquazi, M. Peccianti, L. Razzari, D. J. Moss, S. Coen, M. Erkintalo, Y. K. Chembo, T. Hansson, S. Wabnitz, P. Del'Haye, X. Xue, A. M. Weiner, R. Morandotti, Micro-combs: A novel generation of optical sources. *Phys. Rep.* **729**, 1–81 (2018). doi:10.1016/j.physrep.2017.08.004

3. A. L. Gaeta, M. Lipson, T. J. Kippenberg, Photonic-chip-based frequency combs. *Nat. Photonics* **13**, 158–169 (2019). doi:10.1038/s41566-019-0358-x

4. S. A. Diddams, K. Vahala, T. Udem, Optical frequency combs: Coherently uniting the electromagnetic spectrum. *Science* **369**, eaay3676 (2020). doi:10.1126/science.aay3676 Medline

5. M.-G. Suh, Q.-F. Yang, K. Y. Yang, X. Yi, K. J. Vahala, Microresonator soliton dual-comb spectroscopy. *Science* **354**, 600–603 (2016). doi:10.1126/science.aah6516 Medline

6. D. A. Long, M. J. Cich, C. Mathurin, A. T. Heiniger, G. C. Mathews, A. Frymire, G. B. Rieker, Nanosecond time-resolved dual-comb absorption spectroscopy. *Nat. Photonics* **18**, 127–131 (2024). doi:10.1038/s41566-023-01316-8

7. J. Riemensberger, A. Lukashchuk, M. Karpov, W. Weng, E. Lucas, J. Liu, T. J. Kippenberg, Massively parallel coherent laser ranging using a soliton microcomb. *Nature* **581**, 164–170 (2020). doi:10.1038/s41586-020-2239-3 Medline

8. R. Chen, H. Shu, B. Shen, L. Chang, W. Xie, W. Liao, Z. Tao, J. E. Bowers, X. Wang, Breaking the temporal and frequency congestion of LiDAR by parallel chaos. *Nat. Photonics* **17**, 306–314 (2023). doi:10.1038/s41566-023-01158-4

9. S. A. Miller, Y. Okawachi, S. Ramelow, K. Luke, A. Dutt, A. Farsi, A. L. Gaeta, M. Lipson, Tunable frequency combs based on dual microring resonators. *Opt. Express* **23**, 21527–21540 (2015). doi:10.1364/OE.23.021527 Medline

10. S. Kim, K. Han, C. Wang, J. A. Jaramillo-Villegas, X. Xue, C. Bao, Y. Xuan, D. E. Leaird, A. M. Weiner, M. Qi, Dispersion engineering and frequency comb generation in thin silicon nitride concentric microresonators. *Nat. Commun.* **8**, 372 (2017). doi:10.1038/s41467-017-00491-x Medline

11. H. Bao, A. Cooper, M. Rowley, L. Di Lauro, J. S. Totero Gongora, S. T. Chu, B. E. Little, G.-L. Oppo, R. Morandotti, D. J. Moss, B. Wetzel, M. Peccianti, A. Pasquazi, Laser cavity-soliton microcombs. *Nat. Photonics* **13**, 384–389 (2019). doi:10.1038/s41566-019-0379-5

12. X. Xue, X. Zheng, B. Zhou, Super-efficient temporal solitons in mutually coupled optical cavities. *Nat. Photonics* **13**, 616–622 (2019). doi:10.1038/s41566-019-0436-0

13. Z. Yuan, M. Gao, Y. Yu, H. Wang, W. Jin, Q.-X. Ji, A. Feshali, M. Paniccia, J. Bowers, K. Vahala, Soliton pulse pairs at multiple colours in normal dispersion microresonators. *Nat. Photonics* **17**, 977–983 (2023). doi:10.1038/s41566-023-01257-2

14. J. Vasco, V. Savona, Slow-light frequency combs and dissipative Kerr solitons in coupled-cavity waveguides. *Phys. Rev. Appl.* **12**, 064065 (2019). doi:10.1103/PhysRevApplied.12.064065

15. A. Tikan, J. Riemensberger, K. Komagata, S. Hönl, M. Churaev, C. Skehan, H. Guo, R. N. Wang, J. Liu, P. Seidler, T. J. Kippenberg, Emergent nonlinear phenomena in a driven dissipative photonic dimer. *Nat. Phys.* **17**, 604–610 (2021). doi:10.1038/s41567-020-01159-y

16. A. Tusnin, A. Tikan, K. Komagata, T. J. Kippenberg, Nonlinear dynamics and Kerr frequency comb formation in lattices of coupled microresonators. *Commun. Phys.* **6**, 317 (2023). doi:10.1038/s42005-023-01438-z

17. L. Lu, J. D. Joannopoulos, M. Soljačić, Topological photonics. *Nat. Photonics* **8**, 821–829 (2014). doi:10.1038/nphoton.2014.248

18. T. Ozawa, H. M. Price, A. Amo, N. Goldman, M. Hafezi, L. Lu, M. C. Rechtsman, D. Schuster, J. Simon, O. Zilberberg, I. Carusotto, Topological photonics. *Rev. Mod. Phys.* **91**, 015006 (2019). doi:10.1103/RevModPhys.91.015006

19. H. Price, Y. Chong, A. Khanikaev, H. Schomerus, L. J. Maczewsky, M. Kremer, M. Heinrich, A. Szameit, O. Zilberberg, Y. Yang, B. Zhang, A. Alù, R. Thomale, I. Carusotto, P. St-Jean, A. Amo, A. Dutt, L. Yuan, S. Fan, X. Yin, C. Peng, T. Ozawa, A. Blanco-Redondo, Roadmap on topological photonics. *JPhys Photonics* **4**, 032501 (2022). doi:10.1088/2515-7647/ac4ee4

20. X. Zhang, F. Zangeneh-Nejad, Z.-G. Chen, M.-H. Lu, J. Christensen, A second wave of topological phenomena in photonics and acoustics. *Nature* **618**, 687–697 (2023). doi:10.1038/s41586-023-06163-9 Medline

21. D. Smirnova, D. Leykam, Y. Chong, Y. Kivshar, Nonlinear topological photonics. *Appl. Phys. Rev.* **7**, 021306 (2020). doi:10.1063/1.5142397

22. M. Jalali Mehrabad, S. Mittal, M. Hafezi, Topological photonics: Fundamental concepts, recent developments, and future directions. *Phys. Rev. A* **108**, 040101 (2023). doi:10.1103/PhysRevA.108.040101

23. Z. Wang, Y. Chong, J. D. Joannopoulos, M. Soljacić, Observation of unidirectional backscattering-immune topological electromagnetic states. *Nature* **461**, 772–775 (2009). doi:10.1038/nature08293 Medline

24. M. C. Rechtsman, J. M. Zeuner, Y. Plotnik, Y. Lumer, D. Podolsky, F. Dreisow, S. Nolte, M. Segev, A. Szameit, Photonic Floquet topological insulators. *Nature* **496**, 196–200 (2013). doi:10.1038/nature12066 Medline

25. M. Hafezi, S. Mittal, J. Fan, A. Migdall, J. M. Taylor, Imaging topological edge states in silicon photonics. *Nat. Photonics* **7**, 1001–1005 (2013). doi:10.1038/nphoton.2013.274

26. S. Mittal, J. Fan, S. Faez, A. Migdall, J. M. Taylor, M. Hafezi, Topologically robust transport of photons in a synthetic gauge field. *Phys. Rev. Lett.* **113**, 087403 (2014). doi:10.1103/PhysRevLett.113.087403 Medline

27. S. Barik, A. Karasahin, C. Flower, T. Cai, H. Miyake, W. DeGottardi, M. Hafezi, E. Waks, A topological quantum optics interface. *Science* **359**, 666–668 (2018). doi:10.1126/science.aaq0327 Medline

28. M. Jalali Mehrabad, A. P. Foster, N. J. Martin, R. Dost, E. Clarke, P. K. Patil, M. S. Skolnick, L. R. Wilson, Chiral topological add–drop filter for integrated quantum photonic circuits. *Optica* **10**, 415 (2023). doi:10.1364/OPTICA.481684

29. S. Guddala, F. Komissarenko, S. Kiriushechkina, A. Vakulenko, M. Li, V. M. Menon, A. Alù, A. B. Khanikaev, Topological phonon-polariton funneling in midinfrared metasurfaces. *Science* **374**, 225–227 (2021). doi:10.1126/science.abj5488 Medline

30. J. Guglielmon, M. C. Rechtsman, Broadband topological slow light through higher momentum-space winding. *Phys. Rev. Lett.* **122**, 153904 (2019). doi:10.1103/PhysRevLett.122.153904 Medline

31. M. I. Shalaev, W. Walasik, A. Tsukernik, Y. Xu, N. M. Litchinitser, Robust topologically protected transport in photonic crystals at telecommunication wavelengths. *Nat. Nanotechnol.* **14**, 31–34 (2019). doi:10.1038/s41565-018-0297-6 Medline

32. C. J. Flower, S. Barik, M. Jalali Mehrabad, N. J. Martin, S. Mittal, M. Hafezi, Topological edge mode tapering. *ACS Photonics* **10**, 3502–3507 (2023). doi:10.1021/acsphotonics.3c00463

33. H. Zhao, X. Qiao, T. Wu, B. Midya, S. Longhi, L. Feng, Non-Hermitian topological light steering. *Science* **365**, 1163–1166 (2019). doi:10.1126/science.aay1064 Medline

34. P. St-Jean, V. Goblot, E. Galopin, A. Lemaître, T. Ozawa, L. Le Gratiet, I. Sagnes, J. Bloch, A. Amo, Lasing in topological edge states of a one-dimensional lattice. *Nat. Photonics* **11**, 651–656 (2017). doi:10.1038/s41566-017-0006-2

35. B. Bahari, A. Ndao, F. Vallini, A. El Amili, Y. Fainman, B. Kanté, Nonreciprocal lasing in topological cavities of arbitrary geometries. *Science* **358**, 636–640 (2017). doi:10.1126/science.aao4551 Medline

36. M. A. Bandres, S. Wittek, G. Harari, M. Parto, J. Ren, M. Segev, D. N. Christodoulides, M. Khajavikhan, Topological insulator laser: Experiments. *Science* **359**, eaar4005 (2018). doi:10.1126/science.aar4005 Medline

37. L. Yang, G. Li, X. Gao, L. Lu, Topological-cavity surface-emitting laser. *Nat. Photonics* **16**, 279–283 (2022). doi:10.1038/s41566-022-00972-6

38. V. Peano, M. Houde, F. Marquardt, A. A. Clerk, Topological quantum fluctuations and traveling wave amplifiers. *Phys. Rev. X* **6**, 041026 (2016). doi:10.1103/PhysRevX.6.041026

39. B.-U. Sohn, Y.-X. Huang, J. W. Choi, G. F. R. Chen, D. K. T. Ng, S. A. Yang, D. T. H. Tan, A topological nonlinear parametric amplifier. *Nat. Commun.* **13**, 7218 (2022). doi:10.1038/s41467-022-34979-y Medline

40. S. Mittal, E. A. Goldschmidt, M. Hafezi, A topological source of quantum light. *Nature* **561**, 502–506 (2018). doi:10.1038/s41586-018-0478-3 Medline

41. A. Blanco-Redondo, B. Bell, D. Oren, B. J. Eggleton, M. Segev, Topological protection of biphoton states. *Science* **362**, 568–571 (2018). doi:10.1126/science.aau4296 Medline

42. S. Mittal, V. V. Orre, E. A. Goldschmidt, M. Hafezi, Tunable quantum interference using a topological source of indistinguishable photon pairs. *Nat. Photonics* **15**, 542–548 (2021). doi:10.1038/s41566-021-00810-1

43. T. Dai, Y. Ao, J. Bao, J. Mao, Y. Chi, Z. Fu, Y. You, X. Chen, C. Zhai, B. Tang, Y. Yang, Z. Li, L. Yuan, F. Gao, X. Lin, M. G. Thompson, J. L. O'Brien, Y. Li, X. Hu, Q. Gong, J. Wang, Topologically protected quantum entanglement emitters. *Nat. Photonics* **16**, 248–257 (2022). doi:10.1038/s41566-021-00944-2

44. S. Mittal, G. Moille, K. Srinivasan, Y. K. Chembo, M. Hafezi, Topological frequency combs and nested temporal solitons. *Nat. Phys.* **17**, 1169–1176 (2021). doi:10.1038/s41567-021-01302-3

45. D. Leykam, S. Mittal, M. Hafezi, Y. D. Chong, Reconfigurable topological phases in next-nearest-neighbor coupled resonator lattices. *Phys. Rev. Lett.* **121**, 023901 (2018). doi:10.1103/PhysRevLett.121.023901 Medline

46. S. Mittal, V. V. Orre, D. Leykam, Y. D. Chong, M. Hafezi, Photonic anomalous quantum Hall effect. *Phys. Rev. Lett.* **123**, 043201 (2019). doi:10.1103/PhysRevLett.123.043201 Medline

47. A. Rahim, J. Goyvaerts, B. Szelag, J.-M. Fedeli, P. Absil, T. Aalto, M. Harjanne, C. Littlejohns, G. Reed, G. Winzer, S. Lischke, L. Zimmermann, D. Knoll, D. Geuzebroek, A. Leinse, M. Geiselmann, M. Zervas, H. Jans, A. Stassen, C. Dominguez, P. Munoz, D. Domenech, A. L. Giesecke, M. C. Lemme, R. Baets, Open-access silicon photonics platforms in Europe. *IEEE J. Sel. Top. Quantum Electron.* **25**, 1–18 (2019). doi:10.1109/JSTQE.2019.2915949

48. K. Luke, Y. Okawachi, M. R. E. Lamont, A. L. Gaeta, M. Lipson, Broadband mid-infrared frequency comb generation in a $Si_3N_4$ microresonator. *Opt. Lett.* **40**, 4823–4826 (2015). doi:10.1364/OL.40.004823 Medline

49. T. Fujisawa, S. Makino, T. Sato, K. Saitoh, Low-loss, compact, and fabrication-tolerant Si-wire 90° waveguide bend using clothoid and normal curves for large scale photonic integrated circuits. *Opt. Express* **25**, 9150–9159 (2017). doi:10.1364/OE.25.009150 Medline

50. X. Ji, J. Liu, J. He, R. N. Wang, Z. Qiu, J. Riemensberger, T. J. Kippenberg, Compact, spatial-mode-interaction-free, ultralow-loss, nonlinear photonic integrated circuits. *Commun. Phys.* **5**, 84 (2022). doi:10.1038/s42005-022-00851-0

51. L. D. Tzuang, K. Fang, P. Nussenzveig, S. Fan, M. Lipson, Non-reciprocal phase shift induced by an effective magnetic flux for light. *Nat. Photonics* **8**, 701–705 (2014). doi:10.1038/nphoton.2014.177

52. L. Chang, W. Xie, H. Shu, Q.-F. Yang, B. Shen, A. Boes, J. D. Peters, W. Jin, C. Xiang, S. Liu, G. Moille, S.-P. Yu, X. Wang, K. Srinivasan, S. B. Papp, K. Vahala, J. E. Bowers, Ultra-efficient frequency comb generation in AlGaAs-on-insulator microresonators. *Nat. Commun.* **11**, 1331 (2020). doi:10.1038/s41467-020-15005-5 Medline

53. M. Pu, L. Ottaviano, E. Semenova, K. Yvind, Efficient frequency comb generation in AlGaAs-on-insulator. *Optica* **3**, 823 (2016). doi:10.1364/OPTICA.3.000823

54. M. Zhang, B. Buscaino, C. Wang, A. Shams-Ansari, C. Reimer, R. Zhu, J. M. Kahn, M. Lončar, Broadband electro-optic frequency comb generation in a lithium niobate microring resonator. *Nature* **568**, 373–377 (2019). doi:10.1038/s41586-019-1008-7 Medline

55. M. Jürgensen, S. Mukherjee, M. C. Rechtsman, Quantized nonlinear Thouless pumping. *Nature* **596**, 63–67 (2021). doi:10.1038/s41586-021-03688-9 Medline

56. N. Mostaan, F. Grusdt, N. Goldman, Quantized topological pumping of solitons in nonlinear photonics and ultracold atomic mixtures. *Nat. Commun.* **13**, 5997 (2022). doi:10.1038/s41467-022-33478-4 Medline

57. L. J. Maczewsky, M. Heinrich, M. Kremer, S. K. Ivanov, M. Ehrhardt, F. Martinez, Y. V. Kartashov, V. V. Konotop, L. Torner, D. Bauer, A. Szameit, Nonlinearity-induced photonic topological insulator. *Science* **370**, 701–704 (2020). doi:10.1126/science.abd2033 Medline

58. M. S. Kirsch, Y. Zhang, M. Kremer, L. J. Maczewsky, S. K. Ivanov, Y. V. Kartashov, L. Torner, D. Bauer, A. Szameit, M. Heinrich, Nonlinear second-order photonic topological insulators. *Nat. Phys.* **17**, 995–1000 (2021). doi:10.1038/s41567-021-01275-3

59. C. J. Flower, M. Jalali Mehrabad, L. Xu, G. Moille, D. G. Suarez-Forero, O. Örsel, G. Bahl, Y. Chembo, K. Srinivasan, S. Mittal, M. Hafezi, Observation of Topological Frequency Combs [Dataset], Dryad (2024); https://doi.org/10.5061/dryad.xwdbrv1mw.

60. K. Ikeda, R. E. Saperstein, N. Alic, Y. Fainman, Thermal and Kerr nonlinear properties of plasma-deposited silicon nitride/silicon dioxide waveguides. *Opt. Express* **16**, 12987–12994 (2008). doi:10.1364/OE.16.012987 Medline